LANGMUIR

pubs.acs.org/Langmuir Article

Radial Wicking of Biological Fluids in Paper

Michael J. Hertaeg, Rico F. Tabor, Joseph D. Berry, and Gil Garnier*

Cite This: *Langmuir* 2020, 36, 8209–8217 Read Online

ACCESS | Metrics & More | Article Recommendations | Supporting Information

ABSTRACT: In this study, we analyze stain growth kinetics from droplets of biological fluids such as blood, plasma, and protein solutions on paper both experimentally and numerically. The primary difference of biological fluids from a simple fluid is a significant wetting/dewetting hysteresis in paper. This becomes important in later stages of droplet wicking, after the droplet has been completely absorbed into paper. This is shown by anomalous power dependence of area with time in the later stages of radial wicking. At early stages, current numerical wicking models can predict stain growth of biological fluids. However, at later stages, the introduction of hysteresis complicates modeling significantly. We show that the cause of the observed hysteresis is due to contact angle effects and that this is the dominant mechanism that leads to the anomalous stain growth kinetics measured uniquely in biological fluids. Results presented will streamline the design process of paper-based diagnostics, allowing a modeling approach instead of a trial and error method.

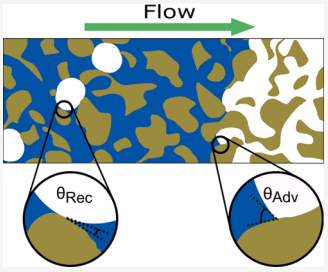

INTRODUCTION

Paper-based diagnostics are integral in an industry-wide shift toward low-cost, point-of-care medical devices. Paper is a flexible platform for these devices because of its low cost and capacity to easily induce passive flows through wicking phenomena caused by capillary forces. Current devices on the market are typically reliant on a trial and error design process because not enough is known about wicking phenomena in paper. While wicking of simple fluids has been well studied as it is integral to many industrial applications including, textiles, printing, agricultural, and medicine,[1−6] wicking of complex fluids has not been studied in depth. This is required for the design of paper-based diagnostics as it will allow the efficient optimization of parameters such as paper properties and geometry. Also, as paper-based devices often involve reactions inside a wicking fluid, a thorough understanding of wicking phenomena is required before any sophisticated reaction optimization can take place. There are critical and distinct differences in the behavior of simple fluids when compared to complex biological fluids and suspensions. Also, the mechanism behind stain growth transition in droplet wicking remains unknown as it has been poorly studied. This lack of understanding is particularly acute for human blood on paper. Much of the literature on the topic is in the field of forensics and is focused on applications rather than fundamental understanding.[7−9]

Biological fluids have many different components that cause complexities. The cell component of blood introduces rheological changes such as a shear-thinning viscosity and granularity caused by the presence of highly deformable red blood cells (RBCs).[10] Also, the significant protein content and lipid component of blood plasma will adsorb onto both solid−liquid and liquid−vapor interfaces, affecting the contact angle, surface tension, and viscosity of the system nonuniformly.[11,12] The most abundant protein in blood is albumin[13] and has been shown to significantly impact wicking in paper.[11]

Wicking is caused by a negative pressure produced by the curved meniscus at the air−liquid interface between pores. The pressure developed in a pore can be approximated with the Young−Laplace equation applied for a capillary with a circular cross section and setting the atmospheric pressure to zero (eq 1)

$$P = -\frac{2\gamma \cos\theta}{R} \tag{1}$$

where P is the pressure on the liquid side of the meniscus, γ is the liquid−vapor surface tension, R is the radius of the capillary, and θ is the contact angle. This negative pressure causes Poiseuille flow toward the meniscus, drawing further fluid into the capillary and moving the interface. In a complex porous material like paper, the pore radius changes depending on position. Therefore, the capillary pressure is not constant and depends on the pore radius. The contact angle at the meniscus is also a critical parameter affecting the driving force.

The radial wicking of a droplet on paper is an example of a complex wicking scenario, and several studies have analyzed stain growth as a function of time.[14−17] In this situation, stain growth continues well after the droplet has absorbed into the paper and disappeared from the surface. The absorption of the drop a finite time after deposition causes a decrease in the spreading rate, which can be clearly identified from the stain

Received: May 5, 2020
Revised: June 18, 2020
Published: June 23, 2020

https://dx.doi.org/10.1021/acs.langmuir.0c01318
Langmuir 2020, 36, 8209−8217

growth kinetics plotted on a log−log scale. The two stages observed are referred to as stage one, where the drop is still present above the paper, and stage two, where the drop has been completely consumed. Before the transition, spreading is driven only by the infiltration of pores near the edge of the stain. After the transition, the reservoir of fluid is consumed and any further stain growth is caused by the redistribution of fluid from the large pores in the center to the unfilled small pores at the edge of the stain. This causes voids to form in the central region, creating receding air interfaces and therefore negative capillary pressures to form within large pores at the center of the stain. This effect causes impedance to further stain growth. At first, the small radius of the filling pores near the edge of the stain dominates and stain growth continues.[18] This becomes less dominant at later times as the meniscus in the center region moves into incrementally smaller pores. Stain growth transition was shown to depend on a hysteresis effect presenting as a difference between infiltration and emptying porous networks.[19] Our previous numerical study showed that including hysteresis is essential to produce clear second-stage transitions and that an increase of hysteresis severity results in a more drastic stage transition.[20] This reveals that the stain growth transition is not caused directly by the consumption of the droplet reservoir. Instead, the stage transition occurs because of a pore hysteresis that only becomes relevant once the droplet is consumed; this is because until this point there are no emptying pores. The cause of this hysteresis is poorly understood and is likely to be material dependent. However, the most likely causes are entrapment due to decreased pore interconnectivity, contact angle hysteresis, and fiber swelling.

It is the objective of this study to elucidate the cause of wetting/dewetting hysteresis in paper and the effect that biological components have on the radial wicking process (Figure 1). This is achieved through experimental analysis of

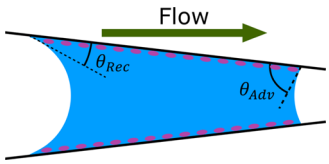

Figure 1. Advancing and receding contact angle in a model capillary with adsorbed biomolecules.

stain growth of biological fluids, contact angle experiments, full-morphology numerical analysis,[21] and continuum-scale modeling using the Richards equation.[22] This work enables the prediction of the wicking behavior of biological fluids for the efficient development of paper diagnostics.

EXPERIMENTAL SECTION

Materials. Cellulose films for contact angle experiments were prepared in the same way as several previous studies.[11,23,24] Here, a 0.5 wt % solution of cellulose acetate (Sigma-Aldrich) in acetone (analytical reagent, Thermo Fisher Scientific) was spin-coated onto glass and then soaked in a 0.5 wt % solution of sodium methoxide (Sigma-Aldrich) in methanol (Analytical reagent, Thermo Fisher Scientific). Whatman 41 filter paper was used for wicking tests, and the blood used was collected with consent by the Red Cross Blood Service Australia following strict ethics requirements. Blood was mixed with ethylenediaminetetraacetic acid (EDTA) as an anticoagulant at collection to prevent coagulation.

Methods. *Experimental Process.* Stain growth data were gathered by monitoring the stain size as a function of time after droplet deposition with the same setup as in our previous study.[20] The bottom view of the paper is captured using a Point Grey Flea3 camera directed onto a 45° mirror positioned underneath the paper. Examples of captured images are shown in Figure 2. Images were

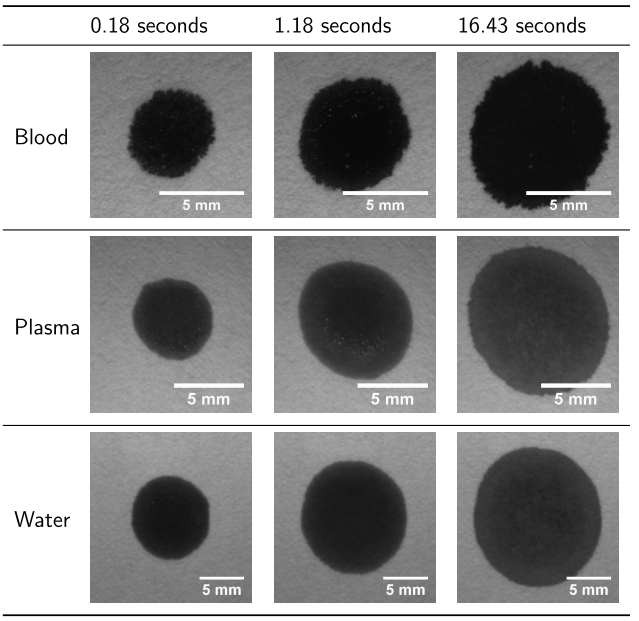

Figure 2. Progression of stains from similar volumes of blood, plasma, and water after droplet deposition on the same paper. Note the different sized scale bars for the different fluids. Droplet volumes: blood 12.9 μL, plasma 13.5 μL, and water 13.8 μL.

taken at a rate of 120 frames/s and analyzed in ImageJ to give area as a function of time. Droplets were created by pumping at a constant flow rate through a needle; this caused droplets of constant size to fall periodically. The size of the droplet was calculated from weight measured using a Mettler Toledo TLE balance before the needle was positioned above the paper. The average weight of the previous four droplets was divided by the fluid's density to estimate the volume of the droplet. The size of the droplet was altered using needles of varying outer diameters. Needles were made by hand by drawing out heated glass capillary tubes. Protein adsorption onto the needle resulted in varying drop volumes. To overcome this, the needles were submersed in the test fluid for 30 min prior to create a saturated layer of adsorbed biomolecules.

Contact angles were measured with an OCA35 Dataphysics contact angle instrument. For advancing and receding measurements, a pump rate of 20 μL/s was used. The presented values are the mean of at least six measurements, and the same batch of cellulose films was used to decrease variability. The static contact angles of blood, plasma, and water on silicon wafers were also measured. Advancing contact angles of water and plasma on cellulose have been previously reported.[11] These were measured and are presented again as a comparison with these new receding measurements with blood components. All wicking and contact angle tests were performed at 23 °C and 50% relative humidity.

The internal structure of the paper used was imaged with a Zeiss Xradia 520 Versa high-resolution X-ray computed tomography scanner. The size of the scan was 150 μm × 150 μm × 205 μm with a resolution of 0.46 μm (voxel volume = 0.46 μm × 0.46 μm × 0.46 μm). The images were binarized in ImageJ using ANKAphase plugin.[25] This plugin implements a phase-contrast algorithm,[26] which was required due to the low absorption of X-rays by cellulose. For analysis, the imaged section is required to be representative of the bulk. For this to be true, the size of the image must be larger than the length scale of heterogeneities in the material. This was confirmed by cropping the image to different sizes and calculating the average

https://dx.doi.org/10.1021/acs.langmuir.0c01318
Langmuir 2020, 36, 8209−8217

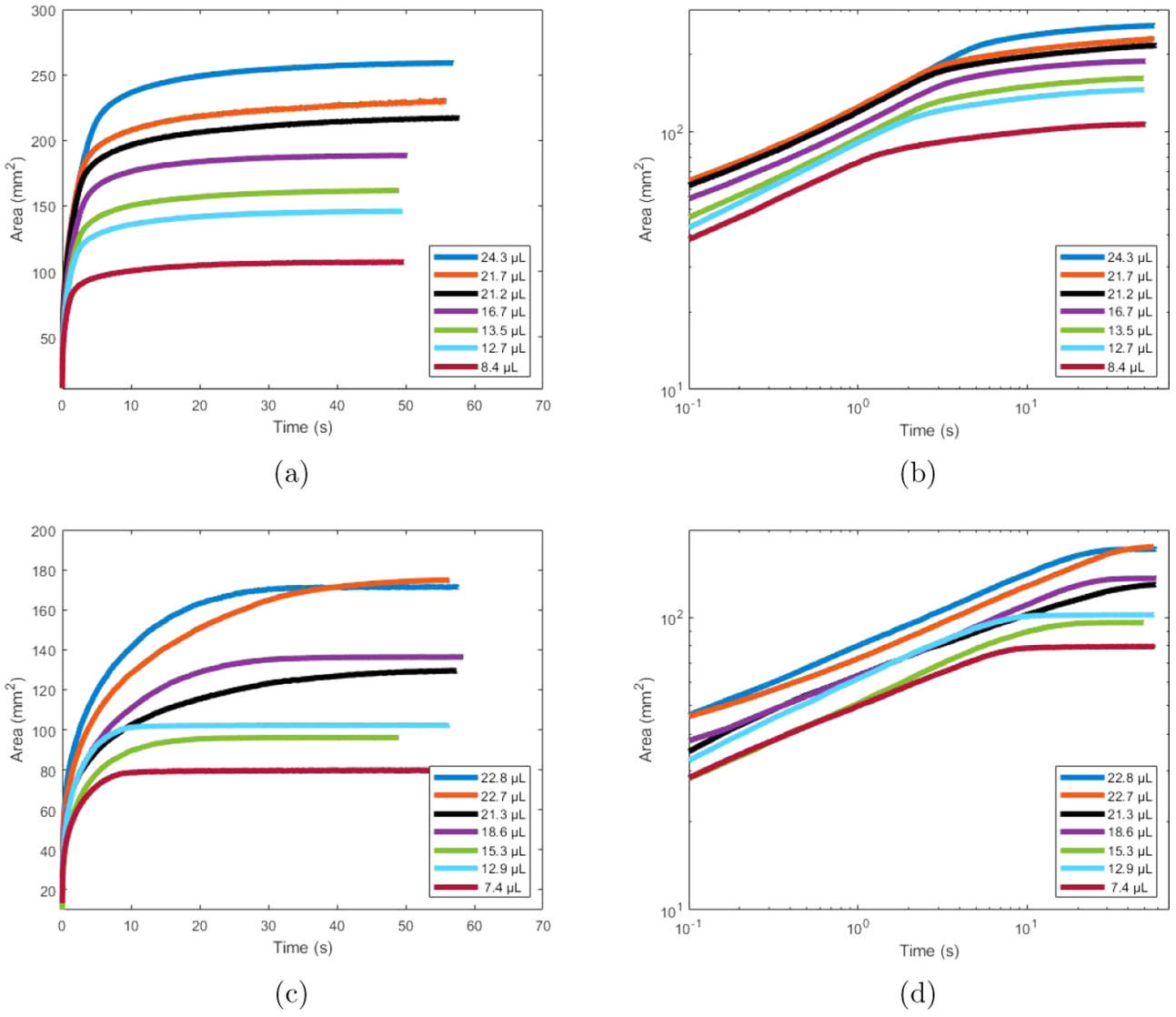

Figure 3. Evolution of stain growth with time for droplets of varying volumes. (a) Plasma linear scale, (b) plasma log scale, (c) blood linear scale, and (d) blood log scale.

volume fraction of the fibers in the new image. As the image size was increased, the average volume fraction plateaued to a constant, indicating that the taken image was large enough to be representative of the bulk properties of the paper.

Numerical Methods. The model selected adopts a similar approach to that of several previous studies.[20,27−29] The Richards equation eq 2 is used to relate volume fraction time and pressure.

$$\frac{\partial \phi}{\partial t} = \nabla \cdot \left(\frac{K(\phi)}{\mu} \nabla P \right) \tag{2}$$

where ϕ is the volume fraction divided by the maximum saturation in the material (ϵ_s), K is the permeability, μ is viscosity, P is pressure, and t is time. In most wicking systems, pressure is a function of only the volume fraction. Due to this, the simpler eq 3 can be used.

$$\frac{\partial \phi}{\partial t} = \nabla \cdot \left(\frac{D(\phi)}{\mu} \nabla \phi \right) \tag{3}$$

where $D(\phi)$ is given by

$$D(\phi) = K(\phi) \frac{\partial P(\phi)}{\partial \phi} \tag{4}$$

$$K(\phi) = K_0 \phi^{(3\lambda+2)/\lambda} \tag{5}$$

$$\frac{\partial P(\phi)}{\partial \phi} = \frac{\gamma \cos \theta P_m}{\lambda} \phi^{(-1-\lambda)/\lambda} \tag{6}$$

Expressions for $K(\phi)$ and $\frac{\partial P(\phi)}{\partial \phi}$ (eqs 5 and 6) can be derived using the Brooks−Coorey model.[30] Equation 6 has been altered to include a linear relationship with surface tension and the cosine of the contact angle. This relationship is predicted from eq 1. These expressions are substituted into eq 4 to give eqs 7 and 8.

λ is the pore distribution index derived from mercury porosimetry or full morphology. In the typical expression derived from the Brooks−Coorey analysis, the product $\frac{\gamma \cos \theta P_m}{\lambda}$ is represented as a single constant, usually defined as the capillary pressure at maximum saturation. This is sometimes set to atmospheric pressure and sometimes left as an empirical constant depending on best fit to data. Here, contributions from surface tension and contact angle on this constant are separated from the contribution from material choice P_m and λ. The effect of P_m is indistinguishable from K_0 in eq 8, so the estimation of this value is not possible. However, both of these constants should be properties of the paper and therefore constant between fluids. Therefore, the product $K_0 P_m$ can be calculated from

https://dx.doi.org/10.1021/acs.langmuir.0c01318
Langmuir 2020, 36, 8209−8217

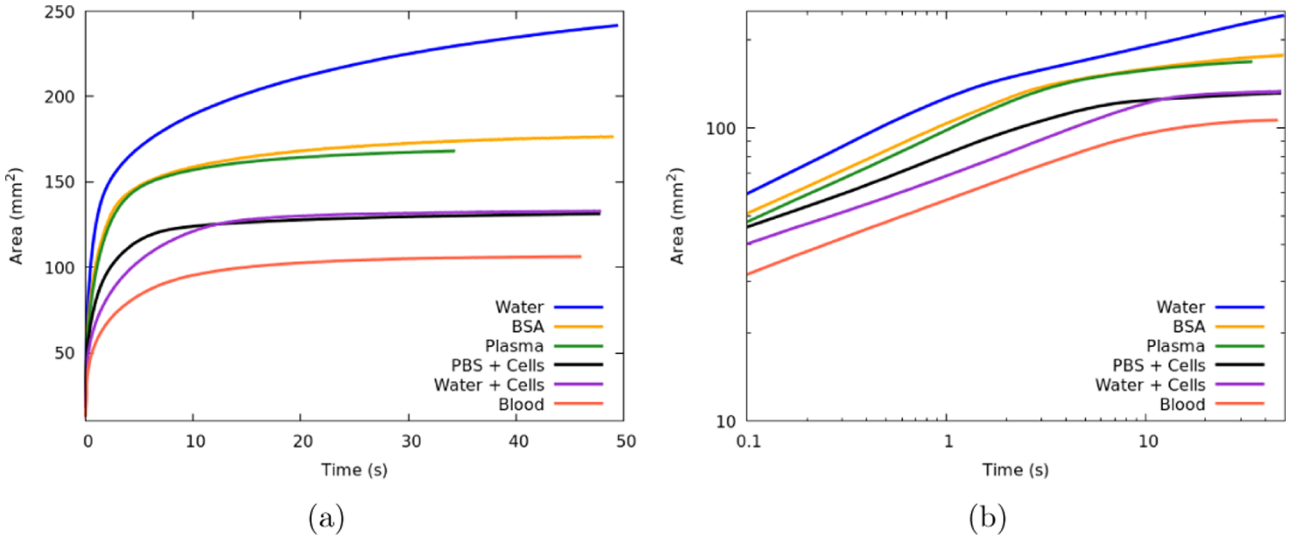

Figure 4. Stain growth of several biofluids interpolated to 15 μL.

experimental data using a single fluid and then used for all fluids on that same paper.

$$D(\phi) = D_0\phi^{(2\lambda+1)/\lambda} \tag{7}$$

$$D_0 = \frac{K_0 P_m \gamma \cos\theta}{\lambda} \tag{8}$$

Once all substitutions have been made, eq 3 is solved using an implicit finite volume method using the open source PDE solver arb[31] over a two-dimensional axisymmetric domain. The same uniform structured mesh and temporal resolution were used as validated in our previous study.[20] $\delta r = 0.02 r_c$ and $\delta t = 0.01$ s, where r_c is the droplet radius. No flux boundary conditions are used on all external faces except for a small region where the droplet is in contact with the paper. Here, a saturated boundary condition is used. The simulation is stopped when the total volume of fluid inside the domain equals the specified volume of the initial droplet. This introduces three additional parameters: the thickness of the paper h, the volume of the droplet V, and the radius of the contact patch r_c. The radius of contact can be estimated using the following equation

$$r_c^3 \approx \frac{3V}{\pi}\left[\frac{\sin^3\theta}{2 - 3\cos\theta + \cos^3\theta}\right] \tag{9}$$

This equation is derived assuming spherical cap geometry on a solid surface. This is not rigorously exact on paper because some of the liquid is absorbed and the instantaneous contact angle over paper will be different from that calculated on other cellulose surfaces due to porosity and roughness. The simplifications introduced in the model mean that the real contact area differs slightly from the effective contact area used in simulations. This is likely caused by ignoring the effects of inertia and dynamic contact angle. Both of these effects have been shown to influence some wicking systems particularly at early times when velocities are high.[32−34] Despite this, eq 9 provides a robust approximation.

Fiber interconnectivity is analyzed with a full-morphology processing step. This is a quasi-static simulation technique to predict the pressure variation in a porous material at various levels of infiltration. It was first developed by Hazlett[21] and has since been used widely to analyze a variety of porous materials, including paper.[28,35] The method uses a three-dimensional (3D) geometry and relies on fitting spheres of constant diameter inside the void space in the geometry. These spheres are allowed to intersect each other but not with the fibers. As the Laplace equation (eq 1) can be used to relate the radius of these spheres to a pressure, the level of infiltration can be calculated as the original nonfiber volume in the paper minus the volume occupied by the overlapping spheres. This is achieved by labeling all voxels occupied by spheres and then adding the volume of all labeled voxels. In this way, the overlap between spheres can be overcome and the true volume of the nonwetting phase calculated accurately. Varying the size of the spheres allows the level of infiltration corresponding to each capillary pressure to be calculated.

Most previous studies have used a commercial implementation of the full-morphology algorithm called GeoDict by Math2Market. For this study, a custom full-morphology implementation was developed and written with Matlab. The code used can be found at https://github.com/MHertaeg/Full-Morphology.git.

RESULTS

Figure 2 demonstrates the stain progression at different times after droplet deposition on the same paper for similar volumes of blood, plasma, and water. Achieving identically sized droplets of different fluids was not possible because fluid surface tension and viscosity affect the volume of droplets generated with a needle. Even from the very early stages of stain growth, blood has a very small stain size followed by plasma and then water. Differences in stain size are highlighted by the change in scale bar length between fluids. There is also a difference between the roughness of the stain boundary of different fluids, clearly forming different fractal dimensions. The highest roughness is seen in blood followed by plasma and water. All stains are slightly elliptical, with the major axis aligned with the paper's machine direction, indicating the expected slight fiber alignment in that direction.

Figure 3 shows the growth of stain area with time from droplets of plasma and blood wicking on filter paper. The log-scale plots are presented, as the gradient of these indicates the power dependence of area with time. These log-scale plots clearly display two typically delineated linear regions.[20] These two regions identify the first and second stages of radial wicking. Although similar in form, blood wicks more slowly than plasma; this is shown by the different vertical scale used to plot the two fluids. It can also be seen that the stage transition occurs much later in blood than in plasma. Discrepancies in blood wicking show that variability is higher between donors with whole blood compared to plasma. This is due to differences in red blood cells between individuals.[36,37] Figure S1 in the Supporting Information shows the variability caused by different donors.

https://dx.doi.org/10.1021/acs.langmuir.0c01318
Langmuir 2020, 36, 8209−8217

Table I. Experimental Contact Angles and Stain Area Powers of Biofluids

fluid	advancing θ_{adv}	receding θ_{rec}	hysteresis $\cos(\theta_{rec}) - \cos(\theta_{adv})$	first-stage power	second-stage power
water	15	5	0.03	0.33 ± 0.11	0.15 ± 0.04
plasma	28	12	0.09	0.32 ± 0.02	0.06 ± 0.01
blood	46	3	0.30	0.24 ± 0.04	≈0

Stain growth tests were also performed with bovine serum albumin (BSA) solution, red cells suspended in phosphate-buffered saline (PBS), and water. This was undertaken to identify the effect cells and protein have on the wicking process. Cells combined with water were tested as this was anticipated to cause a significant number of cells to lyse (burst) driven by a high osmotic pressure difference between the cell and the bulk solution. Albumin is the most abundant protein in blood[13] and therefore serves as a simplified model of plasma. A BSA concentration of 83 g/L BSA in PBS was chosen as it is close to the protein concentration in plasma and has been shown to mimic the wicking behavior of plasma.[11] All red blood cell solutions were prepared at a concentration of 45% by volume to be similar to blood.[38] Stain growth kinetics from all of these fluids are compared to water[20] in Figure 4. As experimental limitations prevented measuring the stain growth from identically sized drops of different fluids, interpolated data must be used. This interpolation was achieved by finding the stain size at every time point and fitting to a linear function of drop volume. Then, using this function, the stain size at any drop volume could be estimated. By combining interpolated stain area data at each time point, the full stain growth plot of any sized droplet could be determined. Figures S1 and S2 in the Supporting Information show the fit of results to linear functions of drop volume for plasma and blood 30 s after droplet deposition. These can be used to demonstrate the small error introduced by this interpolation.

Figure 4 displays a significant difference between the stain growths of the different blood components and water. Pure water wicks very quickly followed by plasma, red blood cell solutions, and then whole blood. Stains from suspensions of blood cells in water and red blood cells in PBS achieve the same equilibrium size. However, red blood cells in water are slightly slower to reach equilibrium. As expected, the behavior of blood plasma is mimicked with the 83 g/L BSA solution. Comparing the gradient of a log−log plot reveals the power dependence of the relationship with time. This value has been quoted in previous studies[15,16] and is very reproducible between results of the same fluid and substrate. The calculated power values for different fluids are shown in Table I. All first-stage powers are similar, but second-stage powers vary significantly. The second-stage power for blood is effectively zero as the stains come to an abrupt halt after a short transition region.

Table I also shows advancing and receding contact angles of water, plasma, and blood on cellulose films. The biological fluids have significantly higher advancing contact angles when compared to water; however, receding angles do not show this trend. The receding angle for blood is lower than all other tested fluids although its difference from water is not significant, particularly considering the inaccuracies in measuring very low contact angles. Contact angle hysteresis is usually presented as a difference in angles. Here, the differences between cosines of the advancing and receding contact angles are displayed in Table I as this is how the contact angle is included in eq 1. This metric is presented to indicate the severity of contact angle hysteresis for these fluids. Plasma produces 3 times the contact angle hysteresis as that of water on cellulose; for blood, it is 10 times. These results demonstrate that there is a correlation between a severe contact angle hysteresis and a low second-stage power. Contact angle measurements for sessile droplets of water, plasma, and blood on silicon wafers were also performed. In this case, all fluids were found to have a similar contact angle of approximately 61°.

Numerical Results. Results of numerical simulations compared to experimental wicking in the first stage for water, plasma, and blood are shown in Figure 5. Good agreement is found apart from the very early stages and the region right before stage transition. The simulations also predict well the timing of the first to second stage transition as the end of simulation results correlates to the position of the change of gradient in the log−log experimental data. The parameters used for each result are shown in Table II. h is the thickness of the paper, ϵ_s is the saturation volume fraction, λ is the pore distribution index, μ is the dynamic viscosity of the fluids, θ is the contact angle, and r_c is the radius of the contact patch of the droplet.

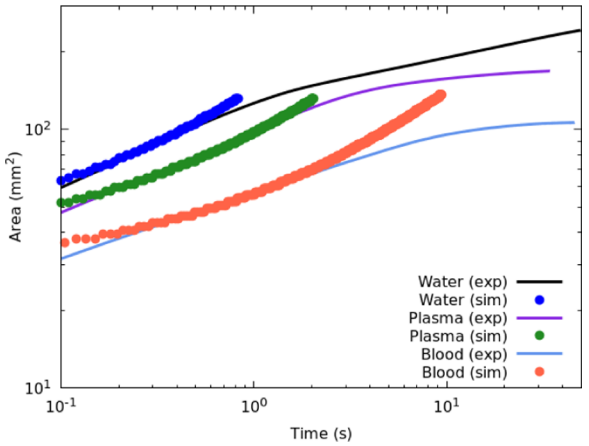

Figure 5. Simulation of the stain area as a function of time on log−log scale results for the first stage of wicking on paper. The parameters of Table II were used with eqs 3, 7, and 8.

Table II. Parameters Used in Figure 5

parameter	water	plasma	blood
V (μL)	15	15	15
μ (mPa·s)	0.93[39]	1.74[11]	4[10]
γ (mN/m)	72.31[40]	60	50
θ (deg)	15	28	46
h (μm)	226[11]	226[11]	226[11]
K_0P_m	8.61×10^{-7}	8.61×10^{-7}	8.61×10^{-7}
r_c (mm)	3.4	3.4	3.1
ϵ_s	0.7[20]	0.7[20]	0.7[20]
λ	5.0[20]	5.0[20]	5.0[20]

https://dx.doi.org/10.1021/acs.langmuir.0c01318
Langmuir 2020, 36, 8209−8217

h, ϵ_s, and λ are properties of the paper and have been calculated or measured in our previous study.[20] The value for K_0P_m was calculated with eq 8 using a previously reported value of D_0.[20] Viscosities are found from the literature. Both blood and plasma have been shown to be shear-thinning;[10] however, as the shear rate in wicking is likely to be very small, a constant viscosity is assumed. θ is the advancing contact angle from Table I.

A few studies have reported the surface tension of blood and plasma. However, the reported values vary significantly.[41−43] This variability could be caused by a number of factors: differences between individuals, use of different anticoagulants in blood collection, different storage conditions, or longer delays between donation and measurement. Variability is also caused by dynamic surface tension due to a transient adsorption of proteins that is rarely considered.[44] Pendant drop surface tensiometry[45] was performed on the samples of whole blood and plasma used in measurements. Due to the quickly changing surface tension right after droplet formation and its dependence on interface dynamics, results were variable. Representative measurements over a large time interval are presented in Figure S3 in the Supporting Information. These correlate with the range of values previously reported. The complex interfacial behavior of such systems means that the surface tension of these fluids will be a function of geometry and diffusion dynamics. Therefore, the effective surface tension in any particular system is difficult to estimate without precise measurements. For this reason, surface tension was fit to data, although the fitted values are within measured ranges for both plasma and blood. Values for r_c are also found by fitting to data. The fitted values are within 20% of the approximate values calculated from eq 9 using the volume of the droplet and the measured contact angle on cellulose.

Full-morphology analysis was performed to assess the effect of liquid entrapment due to insufficient pore interconnectivity and whether this is a primary cause of the observed hysteresis. This is achieved by changing the algorithm to only include a wetting phase infiltration if pores are connected to a wetting phase reservoir at the edge of the domain. This step is common in full-morphology algorithms to account for entrapment of both wetting and nonwetting phases.[46] With this condition included, the current analysis shows negligible change. This implies that the paper pores are sufficiently interconnected to prevent liquid entrapment.

DISCUSSION

Measurements of the stain area as a function of time from several biological fluids are shown in linear and log−log scales in Figure 4. A significant difference in the stain growth kinetics between biological fluids with substantial cell and protein content appears when compared to simple, pure fluids. The second-stage power is strongly system dependent for biological fluids (Table I). Previous numerical research[20] attributed a change in power in the second stage to porosimetry hysteresis. This hysteresis is caused by differences in wetting/dewetting phenomena, and a more severe hysteresis has been shown to cause a lower second-stage gradient. This is because dewetting only occurs when the pores begin to empty after the droplet has been consumed. This occurs at the end of the first stage as the droplet disappears from the surface of the paper. The low second-stage powers exhibited by biological fluids imply that hysteresis is more severe for these fluids. Therefore, to understand the wicking behavior of these complex fluids, the mechanism of porosimetry hysteresis is investigated.

When a droplet is deposited onto the surface of a wettable porous media made of interconnected pores, two phenomena happen concomitantly. The droplet absorbs within the surface and starts wicking along the pores or fibers of the media. Likewise, wicking is a two-step phenomenon dictated by two distinct mechanisms.[17] In the first stage, the pores are filled with fluid provided by the droplet that is slowly being consumed. After some time, the droplet disappears, which initiates the second stage of radial wicking. In this stage, the fluid required to fill pores on the outside of the stain is provided by emptying the larger pores, causing the larger pores to be refilled with air. After the transition, the mechanism responsible for stain growth changes from wetting for the first stage (fluid moving from the droplet into the pores) to a combined wetting/dewetting mechanism for the second[20] (fluid moving from large to small pores). The advancing and receding contact angles drive each process, respectively. Should the advancing and receding angles be similar, or close, such as for decane on paper, a single wicking stage is observed.[20] For most fluids and biological fluids in particular, this is not the case. Wetting and protein adsorption change the three interfacial tensions,[11] thus changing the wetting of an advancing or receding front of the liquid. This means that the advancing angle will be much higher than the receding angle. This affects the driving force behind stain growth and creates the second wicking stage discrepancy discovered in this study.

The developed model can predict the behavior in the first stage. Predictions in Figure 5 deviate from experimental results in the very early stages of stain growth because this region is dominated by effects that are not included in the model. These include inertial and surface impact/wetting effects. As biological fluids show more deviation from the model at early times, this is likely caused by biomolecule adsorption, which brings about dynamic changes in the contact angle, surface tension, and viscosity.[11,44] Results imply that this adsorption has a very short time scale in this system. This is why broad accuracy is achieved using constant parameters. The later stages, right before stage transition, are also not well predicted. This is because in reality, stage transition does not happen instantaneously when the drop is consumed. There is instead a finite time over which the transition occurs. During this transition, the assumptions of constant droplet contact radius and constant saturation are invalid. This is particularly true for blood as the low viscosity and surface tension combined with a high contact angle result in a very slow stage transition that is not captured by this model. Despite these discrepancies, simulation results demonstrate that differences in stain sizes between biological and simple fluids are explained solely by changes in surface tension, contact angle, and viscosity. Continuing the simulation with a shift in boundary conditions to model consumption of the droplet was previously investigated.[20] A good agreement was found for simple fluids; however, such an agreement could not be found for biological fluids. This is likely because hysteresis of contact angles of the wicking fluid is very severe in biological fluids and the simple power law model used previously to account for this in simple fluids is no longer sufficient.

Before a more complete model of second-stage wicking can be derived, the mechanism of porosimetry hysteresis in these systems must be determined and quantified. Three hysteresis

https://dx.doi.org/10.1021/acs.langmuir.0c01318
Langmuir 2020, 36, 8209−8217

mechanisms have been investigated: (1) entrapment in a porous network, (2) fiber swelling, and (3) contact angle hysteresis. The effect of these factors is analyzed below.

In a capillary system, infiltration of the wetting phase will occur only if the nonwetting phase has an evacuation route. Similarly, if a fully wet capillary system is emptied, full evacuation of the wetting phase will not happen unless all wet regions have a path to the applied suction. In paper, the entrapment of liquid could occur during the second stage if initial stages of emptying caused the isolation of small areas of the wetting fluid in isolated areas of smaller pores. This entrapment of fluid in the second stage would produce the observed hysteresis effect.

Full-morphology analysis was used to identify the effect of liquid entrapment. Analysis shows that pores in paper are sufficiently interconnected with a large range of pore sizes such that no entrapment occurs. Thus, limited pore connectivity cannot be the primary cause of the observed hysteresis. This is particularly evident when it is considered that the resolution used would not capture the very small connections caused by fiber overlaps and intrafiber crevices. These very small channels were shown to be partially responsible for fluid transport in paper[47] and would result in a higher than calculated pore connectivity. Figure S4 in the Supporting Information shows the results from full-morphology analysis in comparison to mercury porosimetry measurements fit to the Brooks−Coorey model of pore dynamics.[30] Mercury porosimetry data and model fit are reproduced from a previous study on the same paper.[20] Our full-morphology calculation is similar to model and experimental results. Discrepancies mostly at high and low volume fractions are caused by errors in both full-morphology and mercury porosimetry techniques. The true pressure against the volume fraction curve likely lies in between the two calculated values. Porosimetry results also demonstrate that the majority of the pores in paper are larger than the average size of red blood cells (6 μm).[10] This supports the use of the Richards equation in this system as it implies that blood can be modeled as a continuum.

Another possible cause of the observed hysteresis is paper swelling. This is because swelling fibers effectively consume fluid, removing it from the system and reducing the local pore radius and volume. This decreasing volume of fluid in the system could create a hysteresis effect. This is unlikely as this would not correspond with first-to-second stage transition unless swelling occurred suddenly a finite time after contact. Previous studies showed that the time scale of swelling in normal paper fibers is very short (less than 1 s), so this is unlikely to have an effect.[48] It was also found that a two-stage behavior is still observed in paper made with nonswelling glass fibers.[20] Therefore, swelling is also unlikely to be the cause of hysteresis.

Contact angles experience hysteresis because local physical and chemical heterogeneities produce pinning forces. This could affect the second-stage behavior significantly as the introduction of voids in the center of the stain in this stage creates receding interfaces. Any hysteresis in contact angles would alter the relative magnitude of the capillary pressures at the advancing and receding interfaces. As this is what determines the wicking rate in the second stage, results would likely be affected significantly. Results in Table I show that these systems do experience significant contact angle hysteresis and the trend in hysteresis matches that of the second-stage powers. Therefore, contact angle hysteresis is likely to be the cause of the two-stage behavior measured in radial wicking. This also explains the reported relationship between the contact angle and equilibrium size.[11] Contact angle hysteresis defines the additional resistance to stain growth in the second stage and the anomalous stain kinetics of biological fluids.

Increased advancing contact angle of biological fluids on cellulose has previously been shown to be caused by an increase in solid−liquid interfacial energy due to protein adsorption.[11] The new results presented here show that, in most cases, the receding angle remains low due to pinning forces resisting the triple line motion. These pinning forces could be produced by adsorbed protein and cells at the contact line. This pinning due to adsorbed constituents is commonly observed in many colloid suspensions and would be more severe in blood as compared to plasma. This behavior is matched by experimental results. This implies that the primary cause of the anomalous stain growth behavior of biological fluids is a severe contact angle hysteresis (Figure 1). This occurs because adsorbed biomolecules cause a high advancing contact angle but do not alter the receding angle significantly.

Attempts were made to alter the developed model to incorporate the effects of contact angle hysteresis. This was achieved by including contact angle as a function of the temporal gradient of volume fraction. To do this, eq 3 cannot be used as pressure is no longer solely a function of the volume fraction of fluid in pores. Equation 2 must be selected instead, which requires pressure to be calculated at each cell. A pressure equation can be derived by integrating eq 6; however, this introduces two numerical difficulties. First, the equation predicts a negative infinite pressure at $\phi = 0$; this can be overcome by assuming a linear function of pressure from a threshold minimum volume fraction. This had a negligible effect on results as it maintains the required high pressure gradient over areas with a small volume fraction that was not achieved by simply setting a lower pressure limit. Second, the new pressure field is discontinuous in regions where the temporal gradient of volume fraction changes signs or where the mechanism shifts from filling to emptying. This produces convergence difficulties that could not be resolved. A more detailed numerical study is required to properly resolve the effect of contact angle hysteresis in radial wicking.

The developed model is capable of predicting results in the first stage of wicking for all tested fluids by including values of surface tension, contact angle, and viscosity. This shows that the dynamics for complex fluids in this regime are driven by the same mechanisms as simple fluids.[20,27−29] Results highlight the role of hysteresis in these systems as it is the primary difference between the two stages. For biological fluids, wetting/dewetting hysteresis in the second stage is too severe to model with current techniques. Experimental and numerical investigations show that this hysteresis arises from contact angle effects due to the protein and cell component of the fluids. This identifies why the power relationship with time for these fluids is low.

CONCLUSIONS

In this study, the wicking of biological fluids including human blood, plasma, and protein solutions on paper was measured and modeled from first principles. This was to optimize the design of novel low-cost paper-based diagnostics. A combination of high-speed photography, image processing, and numerical modeling was used. The stain size of biological

https://dx.doi.org/10.1021/acs.langmuir.0c01318
Langmuir 2020, 36, 8209−8217

fluids on paper was recorded as a function of time. A unique second-stage behavior was discovered, differing from that of simple fluids. The two-phase wicking behavior of biological fluids on paper is best visualized by following the stain area as a function of time on a log−log plot. The cause of the second wicking stage of biological fluids is a severe wetting/dewetting hysteresis. Wetting experiments with model systems revealed contact angle hysteresis to be the most likely cause of hysteresis. Fiber swelling and liquid entrapment in porous media were also investigated and dismissed. The difference between first stages exhibited by the different fluids tested was solely driven by differences in viscosity, surface tension, and contact angle. This was demonstrated with a good fit to numerical modeling in the first stage. These results give significant insights into the wicking of biological fluids in paper, particularly in finite reservoir systems where the investigated hysteresis will be significant. This knowledge now enables the development and optimization of a new generation of low-cost diagnostic devices with powerful tools such as computational fluid dynamics and mathematical modeling.

■ ASSOCIATED CONTENT

Supporting Information

The Supporting Information is available free of charge at https://pubs.acs.org/doi/10.1021/acs.langmuir.0c01318.

Fit of linear interpolation to results for plasma (Figure S1); fit of linear interpolation to results for blood (Figure S2); pendant drop tensiometry results for water, plasma, and blood (Figure S3); comparison of full-morphology calculation to mercury porosimetry (Figure S4) (PDF)

■ AUTHOR INFORMATION

Corresponding Author

Gil Garnier − *BioPRIA and Department of Chemical Engineering, Monash University, Clayton, VIC 3800, Australia;* orcid.org/0000-0003-3512-0056; Email: gil.garnier@monash.edu

Authors

Michael J. Hertaeg − *BioPRIA and Department of Chemical Engineering, Monash University, Clayton, VIC 3800, Australia*

Rico F. Tabor − *School of Chemistry, Monash University, Clayton, VIC 3800, Australia;* orcid.org/0000-0003-2926-0095

Joseph D. Berry − *Department of Chemical and Biomolecular Engineering and the Particulate Fluids Processing Centre, University of Melbourne, Parkville, VIC 3052, Australia*

Complete contact information is available at: https://pubs.acs.org/10.1021/acs.langmuir.0c01318

Notes

The authors declare no competing financial interest.

■ ACKNOWLEDGMENTS

This research was funded by an ARC Linkage grant (LP160100544), Haemokinesis, and an Australian Government Research Training Program (RTP) Scholarship. The research was supported in part by Monash eResearch Centre and eSolutions-Research Support Services through the use of the MonARCH HPC Cluster. Thanks to David Paganin for advice on the analysis of X-ray images and the Red Cross Australia for supplying blood products.

■ REFERENCES

(1) Kawase, T.; Sekoguchi, S.; Fujii, T.; Minagawa, M. Spreading of liquids in textile assemblies: Part I: Capillary spreading of liquids. *Text. Res. J.* **1986**, *56*, 409−414.

(2) Khan, M. S.; Thouas, G.; Shen, W.; Whyte, G.; Garnier, G. Paper diagnostic for instantaneous blood typing. *Anal. Chem.* **2010**, *82*, 4158−4164.

(3) Wijaya, M.; Leong, E. C.; Rahardjo, H. Effect of shrinkage on air-entry value of soils. *Soils Found.* **2015**, *55*, 166−180.

(4) Reed, C. M.; Wilson, N. Fundamentals of absorbency of fibres, textile structures and polymers. I: the rate of rise of a liquid in glass capillaries. *J. Phys. D: Appl. Phys.* **1993**, *26*, 1378.

(5) Al-Tamimi, M.; Shen, W.; Zeineddine, R.; Tran, H.; Garnier, G. Validation of paper-based assay for rapid blood typing. *Anal. Chem.* **2012**, *84*, 1661−1668.

(6) Liu, Z.; He, X.; Han, J.; Zhang, X.; Li, F.; Li, A.; Qu, Z.; Xu, F. Liquid wicking behavior in paper-like materials: mathematical models and their emerging biomedical applications. *Microfluid. Nanofluid.* **2018**, *22*, No. 132.

(7) Li, J.; Li, X.; Michielsen, S. Alternative method for determining the original drop volume of bloodstains on knit fabrics. *Forensic Sci. Int.* **2016**, *263*, 194−203.

(8) de Castro, T. C.; Carr, D. J.; Taylor, M. C.; Kieser, J. A.; Duncan, W. Drip bloodstain appearance on inclined apparel fabrics: Effect of prior-laundering, fibre content and fabric structure. *Forensic Sci. Int.* **2016**, *266*, 488−501.

(9) Ramsthaler, F.; Schlote, J.; Wagner, C.; Fiscina, J.; Kettner, M. The ring phenomenon of diluted blood droplets. *Int. J. Leg. Med.* **2016**, *130*, 731−736.

(10) Thiriet, M. *The Biology and Mechanics of Blood Flows*; Springer, 2008.

(11) Hertaeg, M. J.; Tabor, R. F.; Garnier, G. Effect of protein adsorption on the radial wicking of blood droplets in paper. *J. Colloid Interface Sci.* **2018**, *528*, 116−123.

(12) Hagiwara, T.; Nattawut, P.; Shibata, M.; Sakiyama, T. Monitoring of adsorption behaviors of bovine serum albumin onto a stainless steel surface by the quartz crystal microbalance based on admittance analysis. *Biosci., Biotechnol., Biochem.* **2017**, *81*, 783−789.

(13) Greenblatt, D. J. Reduced serum albumin concentration in the elderly: a report from the Boston Collaborative Drug Surveillance Program. *J. Am. Geriatr. Soc.* **1979**, *27*, 20−22.

(14) Gillespie, T. The spreading of low vapor pressure liquids in paper. *Journal of Colloid Science* **1958**, *13*, 32−50.

(15) Kissa, E. Capillary sorption in fibrous assemblies. *J. Colloid Interface Sci.* **1981**, *83*, 265−272.

(16) Danino, D.; Marmur, A. Radial capillary penetration into paper: limited and unlimited liquid reservoirs. *J. Colloid Interface Sci.* **1994**, *166*, 245−250.

(17) Borhan, A.; Rungta, K. K. An experimental study of the radial penetration of liquids in thin porous substrates. *J. Colloid Interface Sci.* **1993**, 403−411.

(18) Marmur, A. Penetration and displacement in capillary systems of limited size. *Adv. Colloid Interface Sci.* **1992**, *39*, 13−33.

(19) Kloubek, J. Hysteresis in porosimetry. *Powder Technol.* **1981**, *29*, 63−73.

(20) Hertaeg, M. J.; Tabor, R. F.; Berry, J. D.; Garnier, G. Dynamics of stain growth from sessile droplets on paper. *J. Colloid Interface Sci.* **2019**, *541*, 312−321.

(21) Hazlett, R. D. Simulation of capillary-dominated displacements in microtomographic images of reservoir rocks. *Transp. Porous Media* **1995**, *20*, 21−35.

(22) Richards, L. A. Capillary conduction of liquids through porous mediums. *J. Appl. Phys.* **1931**, *1*, 318−333.

(23) Huang, Z.; Raghuwanshi, V. S.; Garnier, G. Functionality of immunoglobulin g and immunoglobulin M antibody Physisorbed on cellulosic Films. *Front. Bioeng. Biotechnol.* **2017**, *5*, No. 41.

(24) Su, J.; Garvey, C. J.; Holt, S.; Tabor, R. F.; Winther-Jensen, B.; Batchelor, W.; Garnier, G. Adsorption of cationic polyacrylamide at the cellulose-liquid interface: A neutron reflectometry study. *J. Colloid Interface Sci.* **2015**, *448*, 88−99.
(25) Weitkamp, T.; Haas, D.; Wegrzynek, D.; Rack, A. ANKAphase: software for single-distance phase retrieval from inline X-ray phase-contrast radiographs. Erratum. *J. Synchrotron Radiat.* **2013**, *20*, 205.
(26) Paganin, D.; Mayo, S. C.; Gureyev, T. E.; Miller, P. R.; Wilkins, S. W. Simultaneous phase and amplitude extraction from a single defocused image of a homogeneous object. *J. Microsc.* **2002**, *206*, 33−40.
(27) Perez-Cruz, A.; Stiharu, I.; Dominguez-Gonzalez, A. Two-dimensional model of imbibition into paper-based networks using Richards' equation. *Microfluid. Nanofluid.* **2017**, *21*, No. 98.
(28) Ashari, A.; Bucher, T. M.; Tafreshi, H. V.; Tahir, M. A.; Rahman, M. S. A. Modeling fluid spread in thin fibrous sheets: Effects of fiber orientation. *Int. J. Heat Mass Transfer* **2010**, *53*, 1750−1758.
(29) Jaganathan, S.; Tafreshi, H. V.; Pourdeyhimi, B. A realistic modeling of fluid infiltration in thin fibrous sheets. *J. Appl. Phys.* **2009**, *105*, No. 113522.
(30) Huinink, H. *Fluids in Porous Media*; Morgan & Claypool Publishers, 2016.
(31) Harvie, D. J. E. An implicit finite volume method for arbitrary transport equations. *ANZIAM J.* **2010**, *52*, 1126−1145.
(32) Lavi, B.; Marmur, A.; Bachmann, J. Porous media characterization by the two-liquid method: Effect of dynamic contact angle and inertia. *Langmuir* **2008**, *24*, 1918−1923.
(33) Bosanquet, C. L. V. On the flow of liquids into capillary tubes. *London, Edinburgh Dublin Philos. Mag. J. Sci.* **1923**, *45*, 525−531.
(34) Martic, G.; Gentner, F.; Seveno, D.; Coulon, D.; De Coninck, J.; Blake, T. D. A molecular dynamics simulation of capillary imbibition. *Langmuir* **2002**, *18*, 7971−7976.
(35) Masoodi, R.; Pillai, K. M. *Wicking in Porous Materials: Traditional and Modern Modeling Approaches*; CRC Press, 2012; pp 136−140.
(36) Sala, C.; Ciullo, M.; Lanzara, C.; Nutile, T.; Bione, S.; Massacane, R.; D'Adamo, P.; Gasparini, P.; Toniolo, D.; Camaschella, C. Variation of hemoglobin levels in normal Italian populations from genetic isolates. *Haematologica* **2008**, *93*, 1372−1375.
(37) Ravenhill, B. J.; Kanjee, U.; Ahouidi, A.; Nobre, L.; Williamson, J.; Goldberg, J. M.; Antrobus, R.; Dieye, T.; Duraisingh, M. T.; Weekes, M. P. Quantitative comparative analysis of human erythrocyte surface proteins between individuals from two genetically distinct populations. *Commun. Biol.* **2019**, *2*, No. 350.
(38) Billett, H. H. *Hemoglobin and Hematocrit*, 3rd ed.; Butterworths, 1990.
(39) Kestin, J.; Sokolov, M.; Wakeham, W. A. Viscosity of liquid water in the range- 8 C to 150 C. *J. Phys. Chem. Ref. Data* **1978**, *7*, 941−948.
(40) Vazquez, G.; Alvarez, E.; Navaza, J. M. Surface tension of alcohol water+ water from 20 to 50. degree. C. *J. Chem. Eng. Data* **1995**, *40*, 611−614.
(41) Rosina, J.; Kvasnak, E.; Suta, D.; Kolarova, H.; Malek, J.; Krajci, L. Temperature dependence of blood surface tension. *Physiol. Res.* **2007**, *56*, S93.
(42) Sobac, B.; Brutin, D. Desiccation of a sessile drop of blood: cracks, folds formation and delamination. *Colloids Surf., A* **2014**, *448*, 34−44.
(43) Tarasevich, Y. Y.; Vodolazskaya, I. V.; Bondarenko, O. P. Modeling of spatial-temporal distribution of the components in the drying sessile droplet of biological fluid. *Colloids Surf., A* **2013**, *432*, 99−103.
(44) Zaitsev, S. Dynamic surface tension measurements as general approach to the analysis of animal blood plasma and serum. *Adv. Colloid Interface Sci.* **2016**, *235*, 201−213.
(45) Berry, J. D.; Neeson, M. J.; Dagastine, R. R.; Chan, D. Y. C.; Tabor, R. F. Measurement of surface and interfacial tension using pendant drop tensiometry. *J. Colloid Interface Sci.* **2015**, *454*, 226−237.
(46) Becker, J.; Schulz, V.; Wiegmann, A. Numerical determination of two-phase material parameters of a gas diffusion layer using tomography images. *J. Fuel Cell Sci. Technol.* **2008**, *5*, No. 021006.
(47) Roberts, R.; Senden, T.; Knackstedt, M.; Lyne, M. B.; et al. Spreading of aqueous liquids in unsized papers is by film flow. *J. Pulp Pap. Sci.* **2003**, *29*, 123−131.
(48) Schuchard, D. R.; Berg, J. C. Liquid transport in composite cellulose-superabsorbent fiber networks. *Wood Fiber Sci.* **2007**, *23*, 342−357.

https://dx.doi.org/10.1021/acs.langmuir.0c01318
Langmuir 2020, 36, 8209−8217